

GeV ELECTRON BEAMS FROM A CENTIMETER-SCALE LASER-DRIVEN PLASMA ACCELERATOR

A. J. Gonsalves, K. Nakamura, Cs. Tóth, C. G. R. Geddes, C. B. Schroeder, E. Esarey
 E. Cormier-Michel, W. P. Leemans, LBNL, Berkeley, USA
 D. Bruhwiler, J.R. Cary, Tech-X Corporation, Boulder CO 80303
 S. M. Hooker, Oxford University, Oxford, OX1 3PU, UK

Abstract

Results are presented on the generation of quasi-monoenergetic electron beams with energy up to 1 GeV using a 40 TW laser and a 3.3 cm-long hydrogen-filled capillary discharge waveguide [1, 2]. Electron beams were not observed without a plasma channel, indicating that self-focusing alone could not be relied upon for effective guiding of the laser pulse. Results are presented of the electron beam spectra, and the dependence of the reliability of producing electron beams as a function of laser and plasma parameters.

INTRODUCTION

The accelerating gradient achievable with conventional radio frequency (RF) accelerators is limited by electrical breakdown within the accelerating cavity to a few tens of MeV/m, so the production of energetic beams requires large, expensive accelerators.

To push the energy frontier with devices of practical size will require a technology capable of much higher accelerating gradients. A promising technique is electron acceleration by plasma waves, since these can sustain electric fields of hundreds of GVm^{-1} — 4 orders of magnitude larger than that in a conventional RF linac.

Plasma accelerators not only offer a path to TeV electron beams with relatively small structures, but in the near term, make possible the production of low-cost, laboratory-scale, GeV-class accelerators that can produce femtosecond electron bunches intrinsically synchronized with a laser pulse.

Laser-plasma wakefield accelerators — in which an intense laser beam drives the plasma wave via the ponderomotive force — have produced high-quality 100 MeV electron beams in just a few millimeters [3, 4, 5]. However, until recently, the acceleration length was not sufficient to accelerate electrons to GeV energies. Two key effects that can limit the acceleration length are diffraction of the laser beam and dephasing (electrons outrunning the accelerating region of the wake).

In this paper, the results of experiments demonstrating GeV electron beams from laser-driven plasma accelerators [1, 2] are discussed. A hydrogen-filled capillary discharge waveguide [6, 7, 8] guided high-intensity laser pulses over several centimeters through a plasma of density approximately an order of magnitude lower than in previous laser wakefield experiments. This allowed for the

production of GeV electron beams in a laser-driven plasma accelerator for the first time [1, 2]. Lowering the density was the key, since the linear dephasing length is given by $L_{\text{deph}} = \lambda_p^3 / \lambda^2 \propto n_p^{-3/2}$, where λ_p is the plasma wavelength, λ the laser wavelength, and n_p the plasma density.

EXPERIMENTAL SETUP

The experimental layout is shown in Fig. 1. The laser employed was the LOASIS Ti:sapphire laser at LBNL, which operates at a wavelength of 810 nm and delivered $\tau_{\text{FWHM}} = 40$ fs pulses with a peak power on target of up to 40 TW. The laser pulses were focused onto the entrance of a hydrogen-filled capillary discharge waveguide by a 2 m focal length off-axis paraboloid used at $f/25$ to a spot of size $w_0 = 25 \mu\text{m}$. At full power this focusing geometry corresponds to a peak intensity of $I_0 = 4 \times 10^{18} \text{ Wcm}^{-2}$ and a peak normalized vector potential of $a_0 = 1.4$.

The hydrogen-filled capillary discharge waveguide [6, 7, 8] employed in these experiments used circular capillaries laser-machined into sapphire blocks. Hydrogen was flowed into the capillary via laser-machined grooves near the capillary ends, and a discharge was initiated by using a thyatron switch to connect a charged capacitor across electrodes located at either end of the capillary.

The basic mechanism for channel formation is as follows. The discharge current ionises and heats the plasma, which is cooled at the capillary wall. A temperature profile that is peaked on-axis is formed, and since the pressure gradients are equalised on a timescale much shorter than the period of the discharge, the plasma density increases with distance from the capillary axis.

The energy of electron bunches emerging from the waveguide was measured by an electron spectrometer that used a 1.2 T magnet to deflect the electrons onto a phosphor screen. The phosphor screen was imaged onto four synchronously triggered CCD cameras, enabling single-shot detection of electrons with energies in the ranges 0.03–0.15 and 0.175–1.1 GeV. Electron beam divergence and energy spread were calculated from the data assuming a symmetric electron beam profile and using the imaging properties of the spectrometer, which were obtained from magnetic field maps and a second order electron transport model [9]. Divergence was determined from the e-beam size in the horizontal plane, taking into account the transverse defocusing properties of the magnet. Energy spread

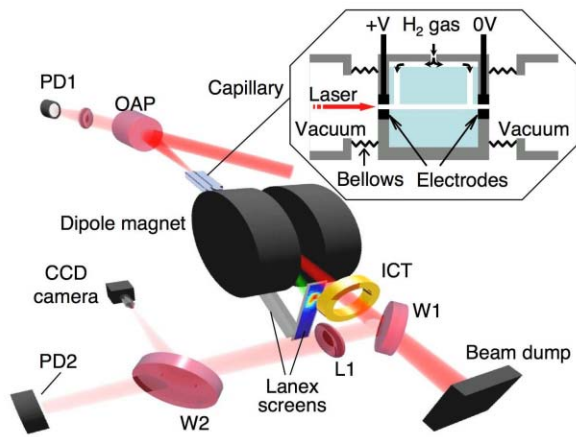


Figure 1: Schematic diagram of the capillary-guided laser wakefield accelerator.

was calculated by deconvolving the effect of finite divergence from the measured e-beam profile. Charge was obtained from a phosphor screen, which was cross-calibrated against an integrating current transformer (ICT).

Optical radiation emerging from the capillary passed through the electron spectrometer and was reflected off two optically flat wedges. The beam was refocused by a lens of focal length 500 mm and diameter 100 mm. Neutral density filters further reduced the beam energy. The image formed by the lens was magnified by a $\times 40$ microscope objective onto a 12-bit CCD camera.

The energy of each laser pulse was measured at the input and output of the waveguide using two photodiodes (PD1 and PD2 in Fig. 1). PD1 was calibrated to the energy on target before the experiment through the use of an energy meter placed between the parabolic mirror and focus. PD2 was cross-calibrated to the first by putting an evacuated beam tube in place instead of the capillary. The delay t between the onset of the discharge and the arrival of the laser pulse, was measured with another photodiode placed behind one of the turning mirrors before the parabolic mirror.

RESULTS

Laser Guiding

Guiding of the laser pulse was optimized by adjusting the initial gas density and the delay t . As shown in Fig. 2a, the laser beam energy transmission correlated with discharge current and — for low power (< 5 TW) — transmission was above 90% for densities ranging from 1.0 to $4.0 \times 10^{18} \text{ cm}^{-3}$ in a 100 ns timing window. Figures 2b and 2c show laser beam profiles at the waveguide entrance and exit for 40 TW laser pulses with an input intensity of $4 \times 10^{18} \text{ Wcm}^{-2}$ and a plasma density of $2.7 \times 10^{18} \text{ cm}^{-3}$. The laser pulse spot size (defined as the radius at which

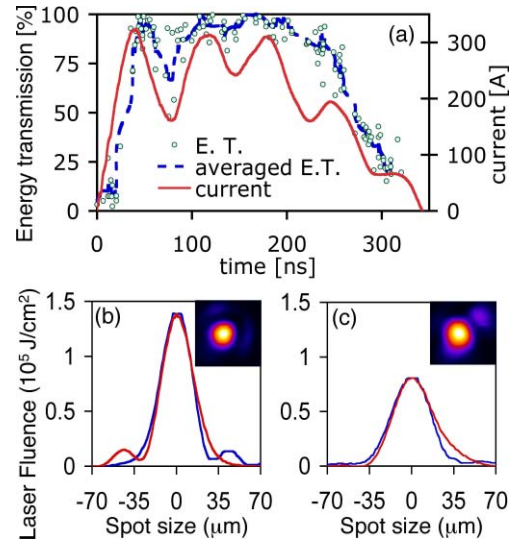


Figure 2: Laser beam energy transmission through the capillary at 5 TW peak input power versus time of arrival of the laser pulse after the onset of the discharge, and mode profiles of the input and output laser beam at 40 TW peak power. The averaged discharge current (red solid line, right axis) and laser pulse energy transmission (green dots, left axis) vs. arrival time of the laser at the capillary for laser pulses < 5 TW are shown in (a). The blue dotted curve is the average transmission. The transverse spatial profiles of laser pulses with an input peak power of 40 TW at the entrance and exit of the 3.3 cm long gas-filled capillary discharge waveguide ($190 \mu\text{m}$ diameter) are shown in (b) and (c), respectively. The blue (red) curve is the horizontal (vertical) lineout.

the peak intensity decreases to $1/e^2$ of its peak value) was $w_0 = 26 \mu\text{m}$ at the entrance and $w_0 = 32 \mu\text{m}$ at the exit. The energy transmission at this laser power dropped to approximately 65%, consistent with transfer of energy to plasma waves and accelerated electrons. Combined with the increase in laser spot size this results in a decrease in laser peak fluence from $1.3 \times 10^5 \text{ Jcm}^{-2}$ to $0.5 \times 10^5 \text{ Jcm}^{-2}$. Assuming that the laser pulse duration remains constant between entrance and exit of the capillary, the peak intensity of the laser was reduced from 3 to $1.2 \times 10^{18} \text{ Wcm}^{-2}$.

The guiding performance was highly sensitive to input beam alignment, with $15 \mu\text{m}$ displacement resulting in transmission drops on the order of 20%. Note that without a preformed plasma channel (laser injected before the onset of the discharge) transmission was below 5% and bulk damage was sustained to the capillary channel walls, indicating that self-ionization and relativistic self-focusing alone could not be relied on for guiding.

Electron Beam Generation

With 12 TW laser power and a plasma density of $3.5 \times 10^{18} \text{ cm}^{-3}$ in a capillary of diameter $225 \mu\text{m}$, every laser

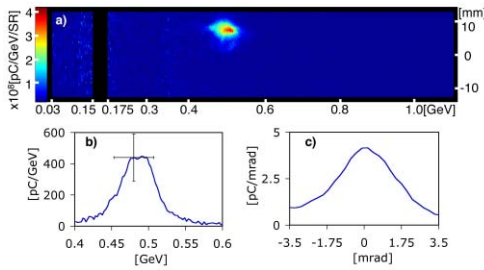


Figure 3: Typical single-shot e-beam spectrum from the stable 0.5 GeV regime of the 225 μm diameter capillary-guided accelerator using a 12 TW laser beam. The image of the dispersed electron beam is shown in (a), the space-integrated spectrum in (b), and the energy-integrated spatial profile in (c). The total charge was 50 pC, and the beam divergence was 2.0 mrad (rms). The energy spread of the beam was estimated to be 5.6% (rms) with resolution of 1.1% (rms). The horizontal error bar in (b) (+0.056, -0.055) comes from the convolution of the uncertainty in the energy (+0.026, -0.024) and the actual fluctuation from measurement (± 0.05) of $0.50_{-0.024}^{+0.026}$ GeV. The vertical error bar in (b) is the convolution of the uncertainty in calibration of the phosphor screen as a charge monitor ($\pm 17\%$) and the actual shot-to-shot fluctuation in charge ($\pm 30\%$), therefore, $\pm 34\%$.

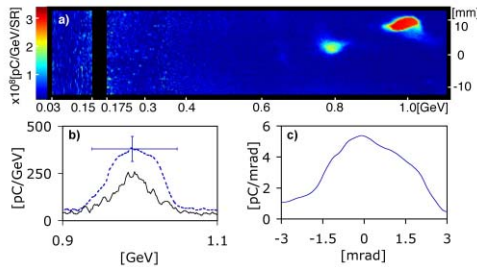


Figure 4: Single-shot e-beam spectrum from a 310 μm diameter capillary-guided accelerator using a 40 TW laser beam. The image of the dispersed electron beam is shown in (a), the space-integrated spectrum (dotted line) in (b), and the energy-integrated spatial profile in (c). The total charge was 30 pC, and the beam divergence was 1.6 mrad (rms). The energy spread of the beam was estimated to be 2.5% (rms) with resolution of 2.4% (rms). The horizontal error bar in (b) comes from the uncertainty in the energy (+0.058, -0.052). The vertical error bar in (b) is due to the uncertainty in calibration of the phosphor screen as a charge monitor ($\pm 17\%$). The solid line in (b) represents the result of the 2D simulation.

shot resulted in an e-beam at 0.48 GeV $\pm 6\%$ and an rms spread 5%, as reported previously [1]. A typical single-shot e-beam spectrum in the stable 0.5 GeV regime is shown in Fig. 3. As stated above, from the energy integrated vertical profile which is shown in Fig. 3 (c), the beam divergence was calculated and used to de-convolve the finite beam ef-

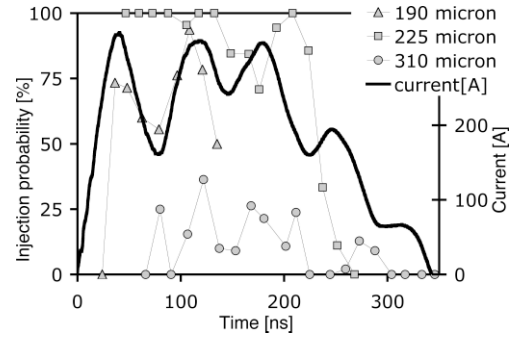


Figure 5: Probability of the observation of electron beams with energy above 30 MeV (left) as a function of the delay between the onset of the current pulse and the arrival of the laser pulse (Solid line, right). Triangles: 190 μm -diameter capillary with $n_e = 3.0 \times 10^{18} \text{ cm}^{-3}$, $E_L = 0.9 \text{ J}$, and $\tau_{\text{FWHM}} = 45 \text{ fs}$. Squares: 225 μm -diameter capillary with $n_e = 3.0 \times 10^{18} \text{ cm}^{-3}$, $E_L = 1.5 \text{ J}$ and $\tau_{\text{FWHM}} = 40 \text{ fs}$. Circles: 310 μm -diameter capillary with $n_e = 4.1 \times 10^{18} \text{ cm}^{-3}$, $E_L = 1.7 \text{ J}$, and $\tau_{\text{FWHM}} = 40 \text{ fs}$. The densities are axial electron densities estimated using equation (1).

fect from space-integrated energy spread, which is shown in Fig. 3 (b). The energy spread of the beam in Fig. 3 is 5.6% rms.

Electron beams with energies of 1 GeV were obtained in a 310 μm diameter capillary for $P = 40 \text{ TW}$ and a density of $4.3 \times 10^{18} \text{ cm}^{-3}$ [1]. A single shot e-beam spectrum with the space-integrated energy profile and energy-integrated spatial profile is shown in Fig. 4. The energy spread was measured to be 2.5% rms, but it may have been less since the resolution of the spectrometer was 2.4%. A spatially displaced second beam is visible at 0.8 GeV. Various mechanisms such as hosing [10], beam loading [11, 12], or dephasing may be responsible for the generation of the second beam. Multi-bunch features of this type were also observed in experiments with the other capillaries, and in numerical simulations owing to trapping of a second electron bunch in a wake bucket behind the first [11, 12]. Electron beams were not observed for lower laser power ($< 38 \text{ TW}$) nor lower plasma density ($\leq 4.0 \times 10^{18} \text{ cm}^{-3}$) in this capillary. The operation of this larger diameter capillary was not as stable as the others (190 μm and 225 μm capillaries), probably due to (a) a greater difference between the spot size of the input laser beam and the matched spot size of the plasma channel, (b) weaker transverse variation of the plasma density leading to a reduction in transverse wavebreaking, and (c) the significance of small variations in the laser and plasma parameters for this high power regime [11].

The solid line shown in Fig. 4 (b) is a simulation performed using the particle-in-cell code VORPAL [13], using 24 grid points per laser wavelength longitudinally, 32 grid points per spot size radially and 4 particles per cell. The best correspondence in 2D was found using a density 20%

higher than the experiment at $5.3 \times 10^{18} \text{ cm}^{-3}$.

Initial 3D simulations at this density show trapping and acceleration of an electron bunch with charge 60 pC, but results of the entire length of the capillary are not yet complete. These simulations show that the laser is self-focused to a spot size of $7 \mu\text{m}$ from an initial size of $25 \mu\text{m}$. This self-focused laser pulse was input to the 2D simulation of the full capillary length.

The 2D simulation shows that the 40 TW, 40 fs laser pulse self-modulates and becomes intense enough to trigger self-trapping after 0.25 cm propagation. The electron bunch accelerates to 1.3 GeV, with 3 % rms energy spread after 0.85 cm of propagation, at which point it begins to dephase. This bunch subsequently outruns the depleted laser pulse and slows to 1.03 GeV with 8 % rms energy spread, approximately 25 pC charge, 2.4 mrad divergence and $30 \mu\text{m}$ spot size at the exit of the plasma channel. The charge is converted from 2D to 3D by assuming that each charge is a ring of the radial size of the beam; the size of the beam before it expands is used, i.e. after 0.8 cm of propagation. It should be noted that 3D simulations are required for a more accurate calculation of beam charge.

Stability of Electron Beam Generation

The threshold laser energy for self-injection of electrons into the plasma wakefield was explored by varying the pumping power of the main amplifier. Focal position changes when adjusting the level of pumping power on the cryogenically cooled amplifier crystal were found to be negligible ($< 0.1 Z_R$) and no spot size changes were observed. The threshold was defined as the minimum energy required to produce electron beams with energy higher than 30 MeV (the lowest energy accepted in the single-shot magnetic spectrometer at full magnetic field strength). The threshold was found to be 0.47 J ($a_0 = 0.75$), 0.68 J ($a_0 = 0.68$), and 1.3 J ($a_0 = 1.3$) for the 190 μm , 225 μm , and 310 μm capillaries respectively. Since the parameter space of density and delay have not been fully explored for the different capillaries, these threshold results should be regarded as tentative. Nevertheless, it seems that the threshold laser energy is lower for smaller capillaries.

Electron beam divergence was also found to depend on capillary diameter. Larger divergence beams were observed from the smaller diameter capillary. From those observations, a possible scenario may be either or both of the following: (a) the fact that the plasma channel has a smaller matched spot for smaller diameter [8] influences the propagation of the laser pulse, which affects injection, and (b) transverse wakefields play a key role in self injection and e-beam properties in the laser-guided LWFA (narrower channels may result in larger transverse density gradients and larger transverse wakefields).

The performance of the accelerator was also found to be sensitive to the delay t , consistent with the observed dependence of the guiding properties. Shown in Fig. 5 is the probability of observing electron beams with energy above

30 MeV (injection probability) as a function of t . For the 190 μm -diameter capillary, an on-axis electron density of $n_e = 3.0 \times 10^{18} \text{ cm}^{-3}$ and a laser beam with energy $E_L = 0.9 \text{ J}$ and a pulse duration of $\tau_{\text{FWHM}} = 45 \text{ fs}$ was used. The injection probability clearly follows the discharge current profile. It should be noted that the probability also depends on the laser parameters and plasma density and can be tuned to achieve 100 % injection. For the 225 μm diameter capillary, the conditions were $n_e = 3.0 \times 10^{18} \text{ cm}^{-3}$, $E_L = 1.5 \text{ J}$, and $\tau_{\text{FWHM}} = 40 \text{ fs}$. Unlike the 190 μm diameter capillary case, injection probability did not follow the ripples on the current, but still showed some temporal structure. Also shown are the results of the 310 μm -diameter capillary using a density of $n_e = 4.1 \times 10^{18} \text{ cm}^{-3}$ and a laser pulse with energy 1.7 J and a pulse duration of 40 fs. Though it is not as clear as the 190 μm diameter capillary case, the injection probability for the 310 μm -diameter capillary weakly follows the temporal structure of the discharge current, having the maximum probability on top of the second ripple and less injection at the local minima of the current profiles. These features are consistent with the temporal dependence of the guiding properties of the waveguide. Also important is that for a discharge current below 50 A, no electron beams were observed.

The dependence of the probability of injection on plasma density was experimentally studied by changing the backing pressure of the hydrogen feed line. The plasma density is then calculated using the results of transverse interferometric experiments [8] that are summarized in Fig. 6, where the measured on-axis electron density is plotted as a function of initial gas density ($n_{\text{H}_2}^i$) for capillaries of various size. Also plotted are the results of a parameter study using fluid simulations [14]. A fit to the measured data yields:

$$n_e(0)[\text{m}^{-3}] = 0.87n_{\text{H}_2}^i[\text{m}^{-3}] + 0.11 \times 10^{24} \quad (1)$$

It can be seen that the measured on-axis electron densities are in good agreement with the scaling given by Brooks *et al.* [14].

The dependence of injection probability on plasma density is plotted in Fig. 7 for the 225 μm -diameter capillary and 310 μm -diameter capillary using a laser beam of energy 1.1 J and 1.5 J respectively. For both cases, it is clear that the probability of injection increases strongly with plasma density.

CONCLUSION

High quality guiding of laser pulses with peak intensity greater than 10^{18} Wcm^{-2} was achieved in a centimeter-scale hydrogen-filled capillary discharge waveguide. This is the longest distance over which laser pulses with intensity greater than 10^{18} Wcm^{-2} have been guided in any type of waveguide — a factor of 10 longer than in previous experiments [4, 15].

Crucially, this increase in the laser-plasma interaction length allowed for the production of electron beams with

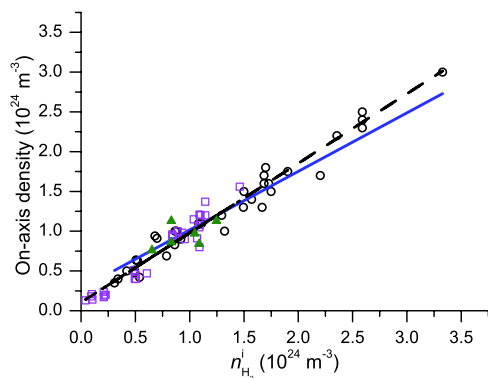


Figure 6: The on-axis electron density as a function of initial density of hydrogen molecules for a capillaries of side 125 μm (triangles), 210 μm (circles), and 465 μm (squares). The dashed line shows a linear fit to the measured data and the solid line shows the dependence deduced from non-LTE fluid simulations [14].

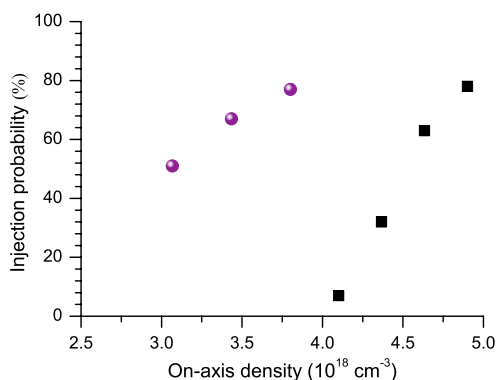


Figure 7: Probability of the observation of electron beams with energy above 30 MeV as a function of on-axis density for capillaries of 225 μm (circles) and 310 μm (squares) diameter for a beam energy of 1.1 J and 1.5 J respectively. The laser pulse length was $\tau_{\text{FWHM}} = 40$ fs in all cases. The probabilities were averaged between 100 ns and 200 ns for the 225 μm -diameter capillary and between 100 ns and 250 ns for the 310 μm -diameter capillary.

energy up to 1 GeV, demonstrating the possibility of a compact GeV-class accelerator based on commercially available high repetition rate laser systems. Beam stability was found to be dependent on discharge-laser delay, density, and laser power. A complete exploration of parameter space, controlled particle injection via laser triggering [16, 17, 18], or density ramp control [19] are expected to result in highly stable performance of this laser-guided laser wakefield accelerator.

REFERENCES

[1] W. P. Leemans, B. Nagler, A. J. Gonsalves, C. Toth, K. Nakamura, C. G. R. Geddes, E. Esarey, C. B. Schroeder, and S. M. Hooker, *Nat Phys* **2**(10), 696 (2006).

[2] K. Nakamura, B. Nagler, C. Toth, C. G. R. Geddes, C. B. Schroeder, E. Esarey, W. P. Leemans, A. J. Gonsalves, and S. M. Hooker, *Physics of Plasmas* **14**(5), 056708 (2007).

[3] S. P. D. Mangles, C. D. Murphy, Z. Najmudin, A. G. R. Thomas, J. L. Collier, A. E. Dangor, E. J. Divall, P. S. Foster, J. G. Gallacher, C. J. Hooker, *et al.*, *Nature* **431**(7008), 535 (2004).

[4] C. G. R. Geddes, C. Toth, J. van Tilborg, E. Esarey, C. B. Schroeder, D. Bruhwiler, C. Nieter, J. Cary, and W. P. Leemans, *Nature* **431**(7008), 538 (2004).

[5] J. Faure, Y. Glinec, A. Pukhov, S. Kiselev, S. Gordienko, E. Lefebvre, J. P. Rousseau, F. Burgy, and V. Malka, *Nature* **431**(7008), 541 (2004).

[6] D. J. Spence, A. Butler, and S. M. Hooker, *Journal of Physics B-Atomic Molecular and Optical Physics* **34**(21), 4103 (2001).

[7] A. Butler, D. J. Spence, and S. M. Hooker, *Physical Review Letters* **89**(18), 185003 (2002).

[8] A. J. Gonsalves, T. P. Rowlands-Rees, B. H. P. Broks, J. J. A. M. van der Mullen, and S. M. Hooker, *Physical Review Letters* **98**(2), 025002 (2007).

[9] K. Makino and M. Berz, *Nuclear Instruments and Methods in Physics Research Section a-Accelerators Spectrometers Detectors and Associated Equipment* **427**(1-2), 338 (1999).

[10] S. Deng, C. D. Barnes, C. E. Clayton, C. O'Connell, F. J. Decker, R. A. Fonseca, C. Huang, M. J. Hogan, R. Iverson, D. K. Johnson, *et al.*, *Physical Review Letters* **96**(4), 045001 (2006).

[11] C. G. R. Geddes, C. Toth, J. van Tilborg, E. Esarey, C. B. Schroeder, D. Bruhwiler, C. Nieter, J. Cary, and W. P. Leemans, *Physics of Plasmas* **12**(5), 538 (2005).

[12] F. S. Tsung, R. Narang, W. B. Mori, C. Joshi, R. A. Fonseca, and L. O. Silva, *Physical Review Letters* **93**(18), 185002 (2004).

[13] C. Nieter and J. R. Cary, *Journal of Computational Physics* **196**(2), 448 (2004).

[14] B. H. P. Broks, W. v. Dijk, and J. J. A. M. v. d. Mullen, *Journal of Physics D: Applied Physics* **39**(11), 2377 (2006).

[15] C. G. R. Geddes, C. Toth, J. van Tilborg, E. Esarey, C. B. Schroeder, J. Cary, and W. P. Leemans, *Physical Review Letters* **95**(14), 145002 (2005).

[16] D. Umstadter, *Laser Focus World* **32**(2), 101 (1996).

[17] E. Esarey, R. F. Hubbard, W. P. Leemans, A. Ting, and P. Sprangle, *Physical Review Letters* **79**(14), 2682 (1997).

[18] J. Faure, C. Rechatin, A. Norlin, A. Lifschitz, Y. Glinec, and V. Malka, *Nature* **444**(7120), 737 (2006).

[19] S. Bulanov, N. Naumova, F. Pegoraro, and J. Sakai, *Physical Review E* **58**(5), R5257 (1998).